

Molecular dynamics simulations reveal the activation mechanism of human TMEM63A induced by lysophosphatidylcholine insertion

Zain Babar, Junaid Wahid, Xiaofei Ji(季晓飞), Huilin Zhao(赵慧琳), Hua Yu(于华), and Dali Wang(王大力)
Citation: Chin. Phys. B, 2025, 34 (**12**): 128704. DOI: 10.1088/1674-1056/ae172d
http://cpb.iphy.ac.cn; http://iopscience.iop.org/cpb

What follows is a list of articles you may be interested in

Mechanical activation of DNA transport across single-walled carbon nanotubes

Junjie Gao(高俊杰), Yichao Wu(吴逸超), Siqi Yu(俞斯棋), Xiaoyan Zhou(周晓艳), and Hangjun Lu(陆杭军)
Chin. Phys. B, 2025, 34 (**10**): 108701. DOI: 10.1088/1674-1056/adce9b

Reconfiguration of B-DNA structure induced by ethanol

Yue Huang(黄悦), Yipeng Chen(陈以鹏), Jing Li(李静), Rongri Tan(谈荣日), and Huanhuan Qiu(邱环环)
Chin. Phys. B, 2025, 34 (**8**): 088707. DOI: 10.1088/1674-1056/adbed9

Molecular simulation study on phase separation of immunoglobulin G

Lv-Meng Hu(胡吕梦), Yuan-Qiang Chen(陈远强), Hong-Ming Ding(丁泓铭), and Yu-Qiang Ma(马余强)
Chin. Phys. B, 2025, 34 (**8**): 088701. DOI: 10.1088/1674-1056/add50b

Depolymerization mechanism of microtubule revealed by nucleotide-dependent changes of longitudinal and lateral interactions

Bingbing Zhang(张冰冰), Ziling Huo(霍子玲), Jiaxi Li(李佳希), Jingyu Qin(覃静宇), and Yizhao Geng(耿轶钊)
Chin. Phys. B, 2025, 34 (**6**): 068702. DOI: 10.1088/1674-1056/adc369

Effects of palmitoylation on membrane protein partitioning into lipid domains in model cellular membranes

Shishi Wu(吴施施) and Qing Liang(梁清)
Chin. Phys. B, 2025, 34 (**5**): 058701. DOI: 10.1088/1674-1056/adbee9

Molecular dynamics simulations reveal the activation mechanism of human TMEM63A induced by lysophosphatidylcholine insertion

Zain Babar[2,†], Junaid Wahid[2,†], Xiaofei Ji(季晓飞)[1], Huilin Zhao(赵慧琳)[1], Hua Yu(于华)[3], and Dali Wang(王大力)[1,‡]

[1] *School of Basic Medical Sciences, Binzhou Medical University, Yantai* 264003, *China*
[2] *School of Foreign Languages and International Exchange, Binzhou Medical University, Yantai* 264003, *China*
[3] *College of Plant Protection, Shandong Agricultural University, Tai'an* 271018, *China*

(Received 30 May 2025; revised manuscript received 30 July 2025; accepted manuscript online 24 October 2025)

OSCA/TMEM63 protein families are recognized as typical mechanosensitive (MS) ion channels in both plants and animals. Resolved OSCA and TMEM63 structures have revealed that these channels are forming dimer and monomer, respectively. Despite the distinguished architectures, OSCA and TMEM63 serve similar functions in multiple physiological processes. Recently, human TMEM63A (hTMEM63A) structure was identified, allowing for investigation into the activation mechanism of hTMEM63A through molecular dynamics (MD) simulations. In this study, we performed multi-scale MD simulations toward hTMEM63A, aiming to reveal how lipid binding regulates hTMEM63A activation. Our results identified two regions on the surface of hTMEM63A, exhibiting a preference for lysophosphatidylcholine (LPC) lipids. Further conformation analyses clarified the activation mechanism of hTMEM63A induced by LPC insertion. These simulation results provide detailed insights into the hTMEM63A–lipid interaction and significant conformational changes associated with hTMEM63A gating, thereby shed lights on the MS ion channel activation mechanism driven by lipid plugging.

Keywords: molecular dynamics simulation, membrane proteins, conformational changes, protein–membrane interactions

PACS: 87.15.ap, 87.14.ep, 87.15.hp, 87.15.kt

DOI: 10.1088/1674-1056/ae172d **CSTR:** 32038.14.CPB.ae172d

1. Introduction

Mechanical sense is one of the fundamental physiological processes that occurs in all organisms.[1] Membrane proteins play a crucial role in sensing external mechanical forces and undergoing conformational changes to transmit these stimuli into cytoplasm.[2] Mechanosensitive (MS) ion channels, one of the force-electric transducers, are widely expressed among prokaryotic and eukaryotic living organisms and are involved in various biological processes, including vascular development, touch, and hearing sensation.[3,4] Based on the paradigms of how MS ion channels respond to the mechanical stimulus, the MS ion channels can be categorized into two types. One of the paradigms is known as 'tether gating model',[5] which includes MS ion channels such as NompC whose ankyrin repeats can sense the mechanical force from the intracellular side.[6–8] Another paradigm is known as 'force from lipid',[9] representing that the MS ion channel can be activated by the force from the bilayer. This activation principle is observed in diverse MS ion channels, involving MS K^+ ion channel TRAAK and TREK,[10–12] bacterial MscL and MscS,[13,14] OSCA in plants,[15–20] and TMEM63 in mammals.[21] Previous research on OSCA families have demonstrated their contributions to plant stem growth and the regulation of turgor pressure, which affects plant-cell size and shape.[22] TMEM63 families, the animal homologous channel families of the plant OSCAs, are proposed to be associated with global development delays and epileptic encephalopathy.[23]

In recent years, we have witnessed the determination of structures of OSCA1.1, OSCA1.2, and OSCA1 from *Arabidopsis thaliana*, revealing that these ion channels adopt a dimeric architecture.[15,16,20] These OSCA channels exhibit a framework that bears resemblance to the calcium activated channel TMEM16, known for its ability to scramble lipids and transport chloride ions.[24] The calcium binding at transmembrane helix M6 of TMEM16 straightens its pore forming helix results in the activation of TMEM16.[25] The cryo-EM structures of OSCA channels have unveiled the presence of a lipid molecule bound to the lower stage of the channel,[19,20] which is considered to be equivalent to the calcium binding of TMEM16.[24] This suggests the binding lipid may be linked to the activation of OSCA channels. Notably, in contrast to the dimeric architecture of OSCA and TMEM16 channels, recent high-resolution TMEM63A structures have revealed its assembly as a monomer.[20,21] Despite this difference, the ar-

[†]These authors contributed equally to this work.
[‡]Corresponding author. E-mail: dlwang@bzmc.edu.cn

© 2025 Chinese Physical Society and IOP Publishing Ltd. All rights, including for text and data mining, AI training, and similar technologies, are reserved.

chitecture of TMEM63A shares similarities with the subunit of dimeric OSCA channels. Moreover, it has also been observed that there is a lipid positioned at the lower stage of TMEM63A channel coordinating to W473, E571, and W613, which is proposed as the critical factor for TMEM63A activation since TMEM63 channels are the animal orthologs to the OSCA channels.

Previous studies have reported that MS ion channels following the 'force from lipid' principle, such as MscS and TRAAK, are dependent on the lipid attachment for their activation. The resolved MscS structures illustrate that lipids block the ion transport pathway as a lock in the channel.[13] In the non-conductive state of TRAAK, the ion transport pathway is obstructed by the lipid tail penetration.[10] Recently, investigations have uncovered that the OSCA channel may be activated under the binding of lyso-lipids, particularly in the lipids anchor sites situated at the extracellular cavity between the two OSCA subunits.[15,20] Given the similarities between TMEM63A and OSCA, an intriguing question arises: is the TMEM63A activation also modulated by lyso-lipid binding? Recent developments in computer hardware and simulation algorithms have established molecular dynamics (MD) simulation as a reliable method for investigating various biological issues.[26–28] In this work, we set up a series of TMEM63A-bilayer systems containing lysophosphatidylcholine (LPC) and phosphatidylinositol bisphosphate (PIP2) and performed multi-scale MD simulations to investigate the specific lipid binding sites along TMEM63A surface and the conformational changes induced by the lipid binding. In the coarse-grained (CG) MD trajectories, we observed that a lipid trapped into the intracellular entrance of the TMEM63A ion pathway with its head group approached the pore forming helices. Further analyses identified two key regions, region I (S538-E539-I542) and region II (D189-N190-D191), which are serving as LPC binding pockets coordinating at the TMEM63A surface, where both the regions are located in proximity to the pore forming helices of TMEM63A. Similar to dimeric MS channel OSCA, the presence of conical lipids such as LPC surrounding TMEM63A likely leads to hydrophobic mismatch, promoting the MS channel gating. Our all-atom (AA) MD simulation results indicate that LPC insertion into the bilayer results in dilation of the upper pore of TMEM63A. In addition to LPC binding residues identified above, we also extracted other vital residues that may directly regulate TMEM63A gating, providing more comprehensive insights into the activation mechanism of ion channels following the 'force from lipid' principle.

2. Results

Specific lipids such as LPC and PIP2 have been reported to attach to the surfaces of ion channels, thereby regulating the behavior of the ion channels. In this work, multiple human TMEM63A (hTMEM63A)-bilayer simulation systems were established with varying bilayer compositions (DPPC:LPC = 4 : 1, DPPC:PIP2 = 4 : 1, DPPC:LPC:PIP2 = 3 : 1 : 1, denoted as 20%LPC, 20%PIP2, and mix, respectively), aiming to investigate the distinct lipid binding regions along the hTMEM63A surface. Figures 1(a)–1(c) show the overview of these init hTMEM63A-bilayer systems. After all the simulations were finished (Figs. 1(d)–2(f)), we first analyzed the root mean squared deviation (RMSD) of hTMEM63A for all the systems. The RMSD values for the 20%LPC systems range from 0.3 nm to 0.45 nm during the latter part of the simulation trajectories (Fig. S1A), while the systems containing PIP2 (20%PIP2 and mix) exhibit smoother fluctuations, with RMSD values hovering around 0.3 nm throughout the trajectories (Figs. S1B&C). The above RMSD analysis results indicate that all the systems were reaching reasonable equilibrium, allowing us to proceed following investigations toward these equilibrated systems.

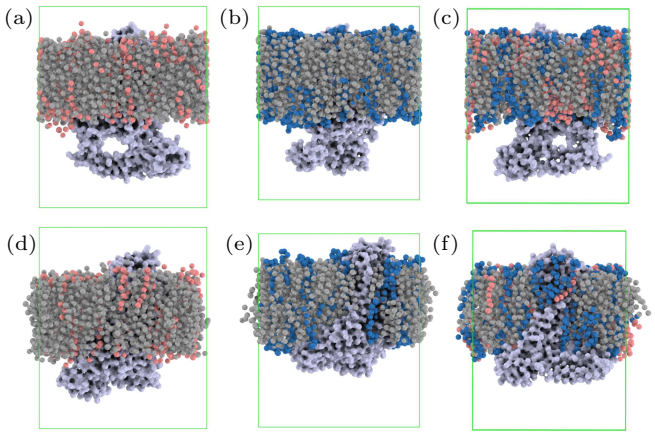


Fig. 1. Overview of hTMEM63A-bilayer systems. Ice blue surface represents MS ion channel hTMEM63A. Lipid DPPC, LPC, PIP2 are shown as grey spheres, pink spheres, and marine spheres, respectively. (a)–(c) Init systems refer to 20%LPC, 20%PIP2 and mix. (d)–(f) System overview of 20%LPC, 20%PIP2 and mix after 1000-ns MD simulation.

The lipid diffusion rate within biological bilayers is affected by multiple factors, including bilayer composition and the presence of membrane proteins. Here, we examine the lipid diffusion properties of two distinct lipid species, LPC and PIP2, in the absence and presence of hTMEM63A embedded within the bilayer. As shown in Figs. 2(a) and 2(b), the diffusion coefficient of LPC is 26.3 ± 2.9 $\mu m^2/s$ when hTMEM63A was embedded in the bilayer, compared to 60.2 ± 6.3 $\mu m^2/s$ in the solo bilayer. Similarly, for PIP2, the diffusion coefficient (Figs. 2(c) and 2(d)) is 13.4 ± 1.3 $\mu m^2/s$ with hTMEM63A embedded, and 42.1 ± 4.8 $\mu m^2/s$ in the absence of the protein. These results indicate that no matter LPC or PIP2, both reflect enhanced diffusion capability when hTMEM63A is absent. A similar trend was also observed in 20%LPC and 20%PIP2 systems (Fig. S2). These findings illuminate that hTMEM63A

insertion inhibits the lipid diffusion along the bilayer, possibly due to the interactions between the protein and the bilayer lipids. Employing the radial distribution function (RDF), we explored neighboring lipid condition around the hTMEM63A. RDF calculations were performed for LPC and PIP2 for hTMEM63A in 20%LPC, 20%PIP2 and mix systems, the results are shown in Figs. S3A-D. The observed convergence of the curves in each panel indicates the reproducibility of lipid distribution across five independent simulations for each system configuration, which demonstrates that the lipids tend to localize within a protein surrounding shell whose radius equals 0.5 nm, corresponding to the first peak in each curve. The above RDF analyses roughly reveal that both LPC and PIP2 are able to accumulate in proximity to the hTMEM63A. To further probe the LPC and PIP2 binding sites along the hTMEM63A surface, we calculated the contact probability of each hTMEM63A residue with LPC and PIP2 molecules. The last 700-ns CG trajectories were extracted for analysis and the results calculated from mix systems are presented in Figs. 2(e) and 2(f), in which Fig. 2(e) displays the value of every residue LPC or PIP2 contact probabilities, while Fig. 2(f) depicts the hTMEM63A 3-D structure colored according to the contact probability value to intuitively visualize the residue distribution. These analyses demonstrate that the majority of hTMEM63A surface residues are occupied by PIP2 molecules, as evidenced by the predominantly blue coloration in Fig. 2(f). Notably, there are still two regions that are able to detect LPC contact signals (highlighted by dashed lines in Fig. 2(e)), indicating these residues exhibit a preference for LPC over PIP2. These LPC-preferential residues are situated close to the pore-forming helices of hTMEM63A, which may trigger pore dilation upon hTMEM63A activation. Overall, the lipid contact probability analysis identifies critical residues involved in lipid–hTMEM63A interactions, providing valuable insights for our subsequent investigations.

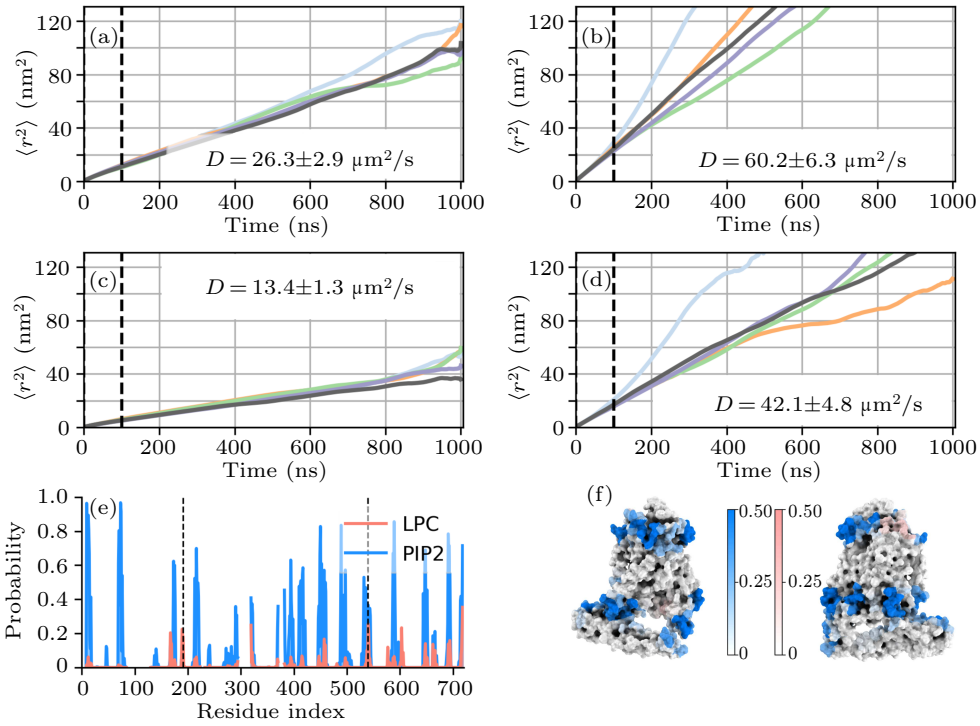


Fig. 2. (a)–(d) The lipid mean squared deviation (MSD) in distinct systems. The dashed lines point out the trajectories that did linear fitting to calculate the diffusion coefficient. (a)–(b) The diffusion coefficient of LPC in mix systems with the presence and absence of hTMEM63A. (c)–(d) same as (a)–(b) but for PIP2. (e) The LPC and PIP2 contact probabilities of hTMEM63A in mix systems. (f) Colored hTMEM63A structure based on the results shown in (e).

The above analyses elucidate that several residues comprise the LPC-binding sites on the hTMEM63A surface, including the residue region S538, E539, I542 (region I) and D189, N190, D191 (region II), which are highlighted in Figs. 2(e) and 2(f). To further investigate the lipid behavior around these two regions, the distance between the nearest LPC lipid and the center of geometry of each region was calculated. The results are presented in Figs. 3 and S4, in which profiles are protruded by bold dots when the distance is less than 0.6 nm. In one of the mix simulations, five LPC molecules were found to be moving around region I (Fig. 3(a)), while four LPC molecules were observed to diffuse towards to region II (Fig. 3(b)), most of them have found their favorite positions and are bound to the hTMEM63A. Following the guidance of the above analyses, typical frames were extracted to intuitively reflect the relative position between the key LPC molecules and hTMEM63A. Figure 3(c) shows the structure after a 500 ns MD simulation, of which one LPC molecule (LPC_1 in Fig. 3(a)) is glued to the region I with comfortable orientation. As the simulation progressed, another LPC molecule (LPC_3 in Fig. 3(a)) moved towards to region I and gradually substituted LPC_1 to fill the region cav-

ity (Fig. 3(d)). Figure 3(e) exhibits the LPC binding posture along region II. The right three panels display the zoom view of the Figs. 3(c)–3(e), respectively. These results provide insights into the molecular interactions between LPC and hTMEM63A, which may contribute to understanding the role that the lipid plays upon hTMEM63A activation processes.

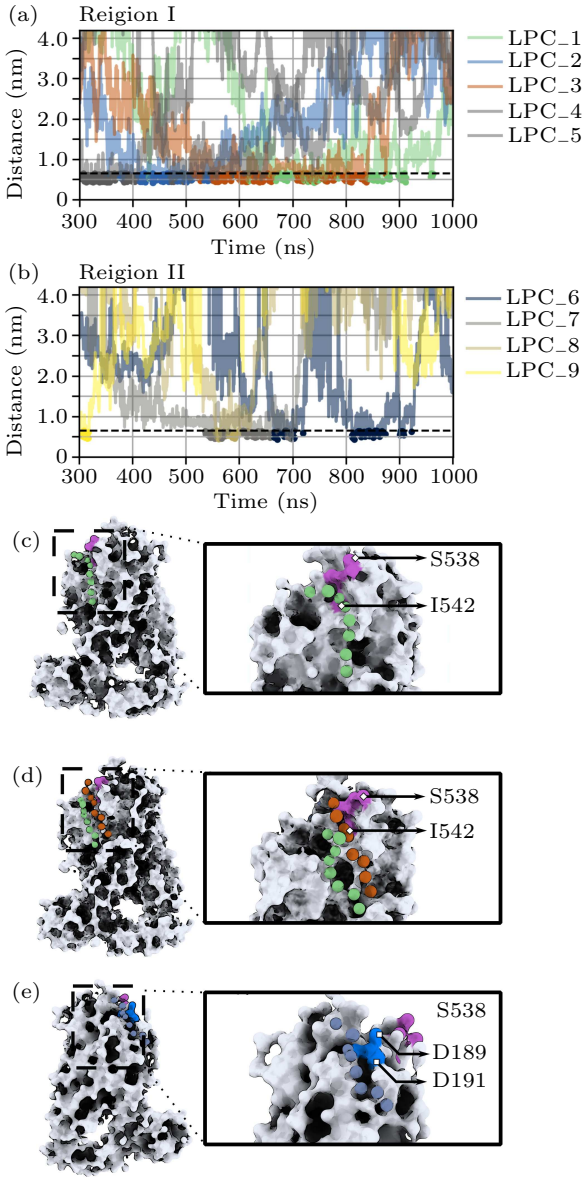


Fig. 3. (a) The distance between the closest LPC molecule and the region I constituted by the residue from S538 to I542. (b) The distance between closest LPC molecule and the region II including D189, N190, and D191. (c) Overview of the LPC_1 orientation binding to region I. The white-grey colored surface represents the hTMEM63A. The magenta highlighting area indicates region I. LPC_1 is painted as pale-green, corresponding to the profile of (a). (d) The snapshot of the LPC_3 is substituting the LPC_1. LPC_3 and LPC_1 are colored by brown and pale-green, respectively. (e) The snapshot of LPC_5 trapped into region II, in which LPC_5 and region II are shown as ice-blue spheres and blue surface, respectively.

Following the CG simulation, we converted the final structure of mix system and proceeded with a series of AA MD simulations. We also conducted an AA MD simulation towards hTMEM63A–DPPC bilayer system (referred to as 'pure' system blow) as a control. Upon completion of the AA MD simulations, the RMSD of each trajectory was calculated. The results, displayed in Fig. S5, show gradual convergence of each profile throughout the simulations, demonstrating the protein conformation of each system has accessed stable state. To compare the conformational changes of hTMEM63A during the simulations, the initial and the final hTMEM63A structure were superposed in Figs. 4(a) and 4(b). As Fig. 4(a) shows, the hTMEM63A conformations between pure (skyblue cartoon representation) and mix (cyan cartoon representation) systems are highly similar before the AA MD simulation. However, after the AA simulation, significant differences were observed in the conformation of hTMEM63A pore-forming helices (highlighted in Fig. 4(b)) between pure and mix trajectories. In Figs. 4(b) and 4(c), it is evident that helix-4 (residue 553-588) in the mix system moves away from helix-6 (residue 461-492), while helix-4 remains nearly unchanged in the pure system. To quantitatively investigate the conformational changes in the both systems, we calculated the distance matrices between residues P461-I482 of helix-4 and residue G553-L573 of helix-6 in the initial and final structures of pure and mix trajectories. To visualize the change in distance more intuitively, the distance deviation (Δdistance) between final and initial structures was analyzed, the results of pure and mix system are shown in Figs. 4(d) and 4(e), respectively. According to the color heat map of Fig. 4(d), we can see that the distance between the top residues of helix-4 and helix-6 extend during the simulations, while the relative distances between other residues remain in the initial status, suggesting that only the extracellular side of hTMEM63A pore enlarges in pure systems. Compared to Fig. 4(d), Fig. 4(e) reveals a broader range of regions where the residues' relative distances become wide, representing the pore-forming helix-4 and helix-6 move apart and induce hTMEM63A pore dilation during the mix simulations. The above analyses have demonstrated hTMEM63A undergoes significant conformational changes during the AA MD simulations. To explore the details of the pore-forming helices motion, we extracted three pairs of residues (Q465–F555, T469–Y559, W473–A562) from helix-4 and helix-6 (Figs. 5(a) and 5(b)). These selected residues are distributed along the ion pathway of hTMEM63A, with their sidechains oriented toward the pore. The distance deviations for these residues are highlighted by three circles in Figs. 4(d) and 4(e). Moreover, how the three distances evolve in the MD simulation is a fancy issue, so we analyzed the Δdistance between each frame and the initial frame. As can be seen in the profiles shown in Fig. 5(c), Δdistance-1 of the pure trajectories gradually extend and maintain the expansive trend during the entire trajectories, while the other two Δdistances do not exhibit significant changes in the simulations, demonstrating that helix-4 does not experience dramatically conformational changes in these trajectories. Conversely, not only is the Δdistance-1 increased in the mix trajectories but both Δdistance-2 and Δdistance-3 also expanded (Fig. 5(d)), indicating that helix-4 moves away from helix-6, resulting in dilation of the hTMEM63A pore radius.

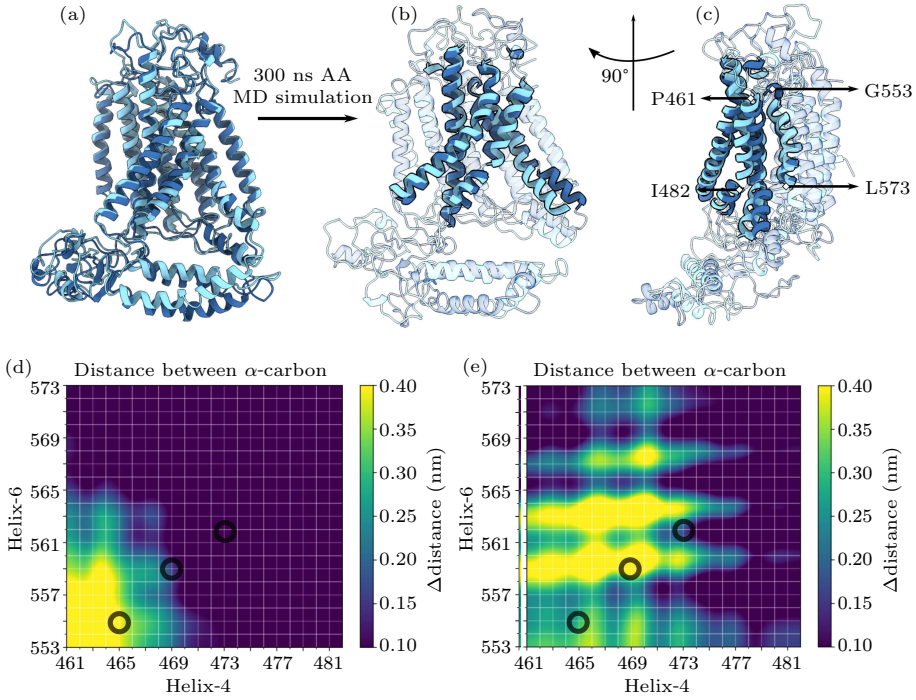


Fig. 4. (a) Alignment of the initial structures of pure (sky-blue ribbons) and mix (cyan ribbons) systems. (b)–(c) Front view and side view of the final structures after AA MD simulations. The pore-forming helices are highlighted and the rest residues are transparent. (d) The distance deviation (Δdistance) calculated between the final structure and the initial structure in pure simulations. The black circles highlight the key interactions between helix-4 and helix-6. (e) Same as (d), but for mix systems.

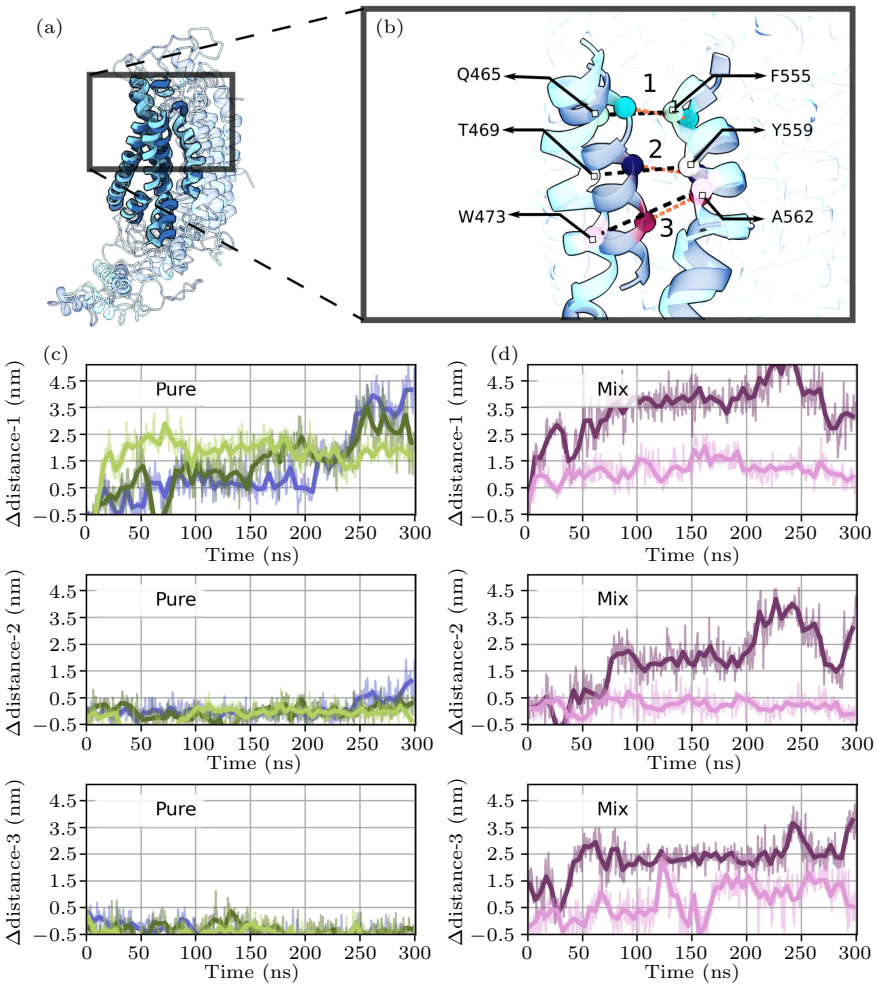


Fig. 5. (a) and (b) The residue positions of the critical hydrophobic interactions highlighted in Figs. 4(d) and 4(e). (c) Δdistance-1, Δdistance-2, Δdistance-3 represent the relative distances between Q465–F555, T469–Y559, W473–A562. The profiles display the Δdistances transformation upon the pure trajectories. (d) Same as (c), but for the mix trajectories.

3. Discussion

In this study, we investigated the diffusion coefficient of LPC and PIP2 molecules in series of CG MD simulations, due to the smoother energy landscape provided by the MARTINI force field, the lipids in the CG simulation exhibit faster diffusion compared to those in the AA force field. Previous studies compared the diffusion coefficient of lipid in CG and atomistic models, demonstrating that the diffusion coefficients of lipids in the CG model can be significantly higher than those in AA model, with a difference of up to 10 times.[29] Based on this correlation, LPC and PIP2 diffusion coefficients in AA model are estimated to be approximately 2.63 ± 0.29 $\mu m^2/s$ and 1.34 ± 0.13 $\mu m^2/s$ in the mix system. These values are comparable to the lipid diffusion coefficient (4–10 $\mu m^2/s$) reported in previous experiments.[30,31] We noticed that LPC diffusion coefficients are almost two times more than PIP2. By combination of our RDF and lipid contact probability analyses, we hypothesized that the distinct diffusion coefficients observed for LPC and PIP2 are attributed to their different protein binding abilities. To preclude the protein impact on the lipid diffusion, we performed a series of CG MD simulations without hTMEM63A. The results reveal that LPC continues to diffuse more rapidly than PIP2, suggesting that the interaction between lipid molecule and hTMEM63A may be one of the reasons influencing the lipid diffusion rate. In addition to protein–lipid interaction, the topology structure of lipids may also play a role in lipid diffusion ability. Distinguished from PIP2, LPC features a single hydrophobic tail, which may facilitate its diffusion in the membrane. In contrast, PIP2 contains a much larger and charged head group, which likely reduces its mobility within the bilayer relative to LPC. Comparing the diffusion coefficients calculated from the systems with and without hTMEM63A, we observed that both LPC and PIP2 reflect enhanced diffusion in the absence of the hTMEM63A. The diffusion coefficients in the sole bilayer system are significantly higher than those in the hTMEM63A-bilayer system, which elucidates the presence of hTMEM63A restricts the motion of both LPC and PIP2. We inferred that hTMEM63A embedding into the bilayer attracts and binds to LPC or PIP2 molecules, reducing their fluidity and consequently lowering their diffusion coefficients.

The above CG MD results identified two distinct regions capable of attracting LPC molecules: region I (S538, E539, I542) and region II (D189, N190, D191). Further sequence alignment analysis (Fig. S6) highlighted that region I, located on the extracellular side of hTMEM63A, is homologous to the lyso-lipid binding residues $P499_{OSCA}$, $N500_{OSCA}$ and $P503_{OSCA}$ of OSCA1.1.[20] Although hTMEM63A topology (monomer) is distinguished from the dimeric OSCA1.1, hTMEM63A shares a similar structure with the single subunit of OSCA1.1 channel, particularly regarding the topology structure of their ion pathways, which are both primarily composed of several transmembrane helices. In addition, the LPC-binding residues in both hTMEM63A and OSCA1.1 are distributed nearly to the extracellular side of the protein ion pathway. As previous work has reported,[15,20] the OSCA channel activation is regulated not only by the lysolipids binding to the extracellular side of its dimer interface but also by the non-conical phosphatidylcholine binding to the bottom entrance of its pore. Another work has revealed that a lipid is present at the lower stage of the ion pathway of the OSCA channel, specifically around $K436_{OSCA}$ and $D524_{OSCA}$.[19] Recent work also identified that lipid could bind to hTMEM63A W473 and W613, which are homologous to OSCA pore residues $K436_{OSCA}$ and $Q573_{OSCA}$.[20] Lipid contact analysis with W473, E571 (homologous to $K436_{OSCA}$, $E532_{OSCA}$) in hTMEM63A revealed that a DPPC molecule (DPPC_1 in Fig. 6(a)) is able to touch these residues (region III). In contrast to the LPC binding regions, only one DPPC molecule remained bound to the region III throughout the simulation trajectories, demonstrating the DPPC molecule has trapped into the region III and prevented its exchange with other lipid. The binding pose of the DPPC molecule, shown in Fig. 6(b), demonstrates that its head group of DPPC_1 has approached close to the W473, with its tail remains embedded into the bilayer. This binding orientation is consistent with the findings reported in the experimental study,[20] in which has discussed the conserved lipid binding mode within OSCA or TMEM63 ion pathway may be functionally analogous to the calcium-binding site identified in the TMEM16 family.

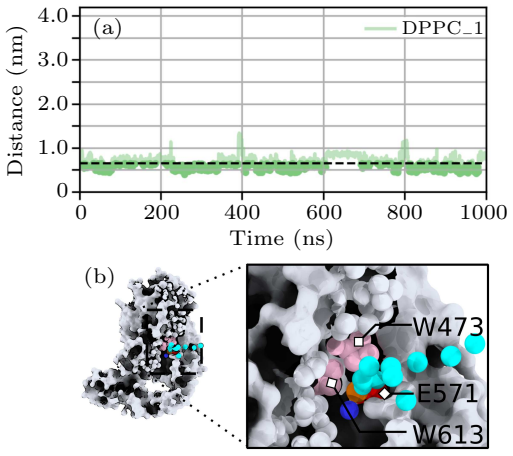


Fig. 6. (a) The distance between the closest lipid and region III (W473, E571 and W613). (b) The related position between the DPPC_1 and region III. The right panel shows a zoom view of the lipid binding pocket located at the intracellular entrance of the hTMEM63A ion pathway.

The AA MD simulations provided more detailed insights into the gating mechanism of hTMEM63A. Our AA MD results indicated a rapid increase in the distance within the upper pore of hTMEM63A during the mix simulations, suggesting the ion pathway of hTMEM63A dilated with LPC insertion. Although the LPC binding regions (S538, E541, I542

and D189, N190, D191) are positioned spatially away from the pore-forming helices, helix-4 and helix-6, similar to OSCA, LPC molecules regulate the channel activation through an allosteric effect. Previous studies have identified the upper pore position as the narrowest section of the OSCA pathway,[15] in which numerous hydrophobic residues are distributed, creating strong hydrophobic interactions that restrict the pore radius. A similar phenomenon was observed in hTMEM63A's ion pathway. In the absence of LPC in the bilayer, only the distance between Q465 and F555 (Δdistance-1) extended, while other hydrophobic interactions remain unaffected during the simulations. As Q465-F555 residue pair is situated at the top entrance of hTMEM63A ion pathway, which is very close to the bulk water. It is logical that hydrophobic interaction between Q465 and F555 can be disrupted without LPC insertion. Contrary to pure systems, the mix systems reflect much differences in Δdistance values, with both Δdistance-2 and Δdistance-3 expanding, leading to an overall extension of the hTMEM63A pore. Comparing the two trajectories in mix systems, represented by the dark pink profiles (mix-1) and light pink profiles (mix-2) in Fig. 5(d), it appears that the pore dilated more dramatically in mix-1 trajectory. All the Δdistance values in mix-1 trajectory fluctuated at higher levels than in the mix-2 trajectory, particularly at the Δdistance-2 position. Figure 5(b) shows the pair of residues T469, Y559 (Δdistance-2) are located in proximity to the hydrophobic core of the upper pore, which is hard to open due to numerous hydrophobic residue distributions. Despite Δdistance-2, Δdistance-3 also exhibits difference between mix-1 and mix-2 (see the bottom panel of Fig. 5(d)). In mix-1 trajectory, the Δdistance-3 enlarged to 2.5 nm and remained stable during the simulation, while Δdistance-3 value in mix-2 trajectory just fluctuated to 2.5 nm and soon shrank to approximately 1.5 nm. The different tendency of Δdistance-3 transformation may influence the gating of Δdistance-2, since the expansion of Δdistance-2 is delayed after the extension of Δdistance-3 extension in the mix-1 simulation. We infer that the dilation of Δdistance-3 is the precondition for the opening of Δdistance-2. The increase in Δdistance-3 reflects the separation of W473 from A562, disrupting the hydrophobic interactions in the upper pore of hTMEM63A. W473 also serves as the non-conical lipid binding site of hTMEM63A,[20] and the lipid binding may facilitate the outward motion of W473. Furthermore, the conformational change of W473 is able to reduce the hydrophobicity in the upper pore of hTMEM63A, thereby promoting the disruption of the hydrophobic core and inducing further activation of hTMEM63A. Collectively, our AA MD results reveal that the gating of hTMEM63A is regulated by two critical hydrophobic locks, T469-Y559 and W473-A562. The T469-Y559 interaction is more tightly bound, and its dilation requires the disruption of the interaction between W473 and A562.

4. Conclusion

In this work, multi-scale MD simulations were employed to investigate the activation mechanism of hTMEM63A. Lipid behavior analysis identified two LPC binding regions located along the surface of hTMEM63A. Further AA MD simulations revealed the disruption of two key hydrophobic interactions (T469-Y559 and W473-A562) within the upper pore of hTMEM63A plays a crucial role in its activation. Notably, the interruption of W473-A562 is more substantial, which may facilitate the opening of T469-Y559. These findings not only provide theoretical guidance for further research towards the detailed mechanism of hTMEM63A activation but also offer a reliable reference for future investigations that the ion channels shared similar architecture with hTMEM63A.

5. Methods

5.1. Coarse-grained molecular dynamics simulation systems set up

All the MD simulation trajectories were obtained under Gromacs 2020.5[32] with MARTINI force field.[33,34] The cyro-EM structure of hTMEM63A,[20] PDBID: 8GRS, was downloaded from Protein Data Bank to serve as the initial structure for the CG MD simulations. The structures and corresponding topology files for simulation were generated by the script *marinize.py*.[34,35] The bilayers we adopted in this work were mainly composed of 1,2-dipalmitoyl-sn-glycero-3-phosphorylcholine (DPPC), in addition with LPC or phosphatidylinositol bisphosphate (PIP2), the ratio of these component is DPPC:LPC = 4:1 (20%LPC), DPPC:PIP2 = 4:1 (20%PIP2), DPPC:LPC:PIP2 = 3:1:1 (mix). Script *insane.py* was utilized to put the lipid around hTMEM63A with a bilayer shape. The sole bilayer ratio is coincide with the corresponding hTMEM63A-bilayer systems, using *insane.py* to place the lipid molecules forming as a bilayer shape. Finally, both the hTMEM63A-bilayer structure and sole bilayer structure were solvated into a $10 \times 10 \times 12$ nm^3 water box, respectively. Na^+ and Cl^- ions were added to neutralize the systems. The detailed compositions of all the systems are shown in Table S1.

5.2. Coarse-grained molecular dynamics simulation

Prior to conducting MDs simulations for production, we equilibrated the systems to eliminate irrational contacts and achieve the desired target conditions. The systems were first energy minimized for 5000 steps, followed by 0.5-ns NVT (canonical ensemble) equilibration, performed with a time step of 20 fs. After equilibration, the systems' temperature and pressure reached 310 K and 1.0 bar. Among each system, five 1000-ns independent simulations were conducted under the NPT ensemble (isothermal-isobaric ensemble), of which the time steps were set to 20 fs. The V-rescale algorithm was employed to maintain the system temperature at 310 K.[36]

The Berendsen algorithm was used to maintain the pressure at 1.0 bar and the pressure coupling type was set to semi-isotropic.[37] Both temperature coupling and pressure coupling constant were 1.0 ps. The electrostatic interactions were calculated with the reaction-field method. While van der Waals interaction was cut off at a distance of 1.1 nm. The elastic network with a force constant of 1000 kJ/mol/nm^2 and a cutoff distance of 1 nm was applied to the protein to preserve its conformation during the simulation. Additionally, the LINCS (linear constraint solver) was implemented for bond constraints.[38]

5.3. All-atom molecular dynamics simulation

After CG MDs simulation finished, the final structures with pure DPPC bilayer and mix bilayer were converted to atomistic model in CHARMM36m force field,[39] serving as subsequent AA MD initial structures. After the 5000-step energy minimization, the system was equilibrated for 0.5 ns in the NVT ensemble and 1.5 ns in the NPT ensemble, with the position restraints towards heavy atoms of hTMEM63A gradually reduced from 2000 kJ/mol/nm^2 to 50 kJ/mol/nm^2. The lipid molecules were also constrained with the force constant gradually reduced from 1000 kJ/mol/nm^2 to 0. At the equilibrated stage, v-rescale[36] and Berendsen[37] algorithms were used to maintain the system temperature at 310 K and system pressure at 1.0 bar, respectively. Both the coupling constants were set to 1.0 ps. The cutoff distance of van der Waals interactions was 1.0 nm, which is switched off from 1.0 nm to 1.2 nm. The particle-mesh-Ewald (PME) algorithm was utilized to calculate the long-range electrostatic interactions.[40] After the equilibration, all of the position restraints were removed and 3×300 ns trajectories of hTMEM63A-dppc system (pure) and 2×300 ns trajectories of hTMEM63A-mix system (mix) were performed. At the production stage, the pressure coupling algorithm was set to Parrinello–Rahman[41] to maintain the system pressure.

5.4. Data analysis

5.4.1. Diffusion coefficient calculation

The mean squared deviations (MSDs) of lipids were calculated by Gromacs built-in analysis tool, gmx_msd. The lipid motion in the bilayer can be considered as the two-dimensional diffusion, in which the relationship between the MSD ($\langle r^2 \rangle$) and the simulation time can be represented in the following equation:

$$\langle r^2 \rangle = 4Dt, \tag{1}$$

where t is the simulation time and D is the lipid diffusion coefficient. We extracted the first 100-ns trajectories to do the linear fitting to obtain the lipid diffusion coefficient.

5.4.2. Lipid contact probability

The protein–lipid interactions are considered when the distance between the protein residue and lipid head group is less than 6 Å. Based on the above lipid diffusion coefficient and protein RMSD analysis, the protein and lipids find their favorable configurations during the initial 300-ns simulation trajectories. Consequently, the first 300-ns trajectories were excluded from the following lipid–protein interaction analysis. We quantified the frames (frames_interact) in which generic lipid L can interact with protein residue R in the final 700-ns trajectory. Then, the ratio between the frames_interact and total frames of the trajectory (frames_total) was calculated to access the probability that residue R contacts with the lipid L.

Data availability statement

The data that support the findings of this study are available from the corresponding author upon reasonable request.

Acknowledgements

This work was supported by the Natural Science Foundation of Shandong Province (Grant Nos. ZR2024QC388 and ZR2023MH101) and Science and Technology Support Plan for Youth Innovation of Colleges and Universities of Shandong Province (Grant No. 2020KJK006). The work was carried out at National Supercomputer Center in Tianjin, and the calculations were performed on Tianhe new generation supercomputer.

References

[1] Kefauver J M, Ward A B and Patapoutian A 2020 *Nature* **587** 567
[2] Jin P, Jan L Y and Jan Y N 2020 *Annual Review of Neuroscience* **43** 207
[3] Douguet D and Honoré E 2019 *Cell* **179** 340
[4] Blount P and Iscla I 2020 *Microbiology and Molecular Biology Reviews* **84** 19
[5] Zhang W, Cheng L E, Kittelmann M, Li J, Petkovic M, Cheng T, Jin P, Guo Z, Göpfert M C, Jan L Y and Jan Y N 2015 *Cell* **162** 1391
[6] Zhang W, Yan Z, Jan L Y and Jan Y N 2013 *Proc. Natl. Acad. Sci. USA* **110** 13612
[7] Jin P, Bulkley D, Guo Y, Zhang W, Guo Z, Huynh W, Wu S, Meltzer S, Cheng T, Jan L Y, Jan Y N and Cheng Y 2017 *Nature* **547** 118
[8] Wang Y, Guo Y, Li G, Liu C, Wang L, Zhang A, Yan Z and Song C 2021 *eLife* **10** 1
[9] Ridone P, Grage S L, Patkunarajah A, Battle A R, Ulrich A S and Martinac B 2018 *Journal of the Mechanical Behavior of Biomedical Materials* **79** 158
[10] Brohawn S G, Campbell E B and MacKinnon R 2014 *Nature* **516** 126
[11] Aryal P, Jarerattanachat V, Clausen M V, Schewe M, McClenaghan C, Argent L, Conrad L J, Dong Y Y, Pike A C, Carpenter E P, Baukrowitz T, Sansom M S and Tucker S J 2017 *Structure* **25** 708
[12] Clausen M V, Jarerattanachat V, Carpenter E P, Sansom M S and Tucker S J 2017 *Proc. Natl. Acad. Sci. USA* **114** E8343
[13] Zhang Y, Daday C, Gu R X, Cox C D, Martinac B, de Groot B L and Walz T 2021 *Nature* **590** 509
[14] Bootha I R and Blount P 2012 *Journal of Bacteriology* **194** 4802
[15] Zhang M, Wang D, Kang Y, Wu J X, Yao F, Pan C, Yan Z, Song C and Chen L 2018 *Nature Structural & Molecular Biology* **25** 850
[16] Liu X, Wang J and Sun L 2018 *Nat. Commun.* **9** 1

[17] Maity K, Heumann J M, McGrath A P, Kopcho N J, Hsu P K, Lee C W, Mapes J H, Garza D, Krishnan S, Morgan G P, Hendargo K J, Klose T, Rees S D, Medrano-Soto A, Saier M H, Piñeros M, Komives E A, Schroeder J I, Chang G and Stowell M H 2019 *Proc. Natl. Acad. Sci. USA* **116** 14309

[18] Swetha E M, Adrienne E D, Tess Whitwam, Sebastian Jojoa-Cruz, Stuart M C, Seyed Reza M, Andrew B Ward and Ardem Patapoutian 2018 *eLife* **7** e41844

[19] Jojoa-Cruz S, Saotome K, Murthy S E, Tsui C C A, Sansom M S, Patapoutian A and Ward A B 2018 *eLife* **7** 1

[20] Zhang M, Shan Y, Cox C D and Pei D 2023 *Nat. Commun.* **14** 1

[21] Zheng W, Rawson S, Shen Z, Tamilselvan E, Smith H E, Halford J, Shen C, Murthy S E, Ulbrich M H, Sotomayor M, Fu T M and Holt J R 2023 *Neuron* **111** 3195

[22] Hamant O and Haswell E S 2017 *BMC Biology* **15** 1

[23] Fukumura S, Hiraide T, Yamamoto A, Tsuchida K, Aoto K, Nakashima M and Saitsu H 2022 *Brain and Development* **44** 178

[24] Dang S, Feng S, Tien J, Peters C J, Bulkley D, Lolicato M, Zhao J, Zuberbühler K, Ye W, Qi L, Chen T, Craik C S, Jan Y N, Minor D L, Cheng Y and Jan L Y 2017 *Nature* **552** 426

[25] Paulino C, Kalienkova V, Lam A K, Neldner Y and Dutzler R 2017 *Nature* **552** 421

[26] Tan R, Xia K, Xun D, Zong W and Yu Y 2023 *Chin. Phys. B* **32** 128703

[27] Tang Y, Yang Z, Yao Y, Zhou Y, Tan Y, Wang Z, Pan T, Xiong R, Sun J and Wei G 2024 *Chin. Phys. B* **33** 030701

[28] Zhang B W, Zhang B Q, Shao Z G and Wu X 2024 *Chin. Phys. B* **33** 118102

[29] Ermakova E and Zuev Y 2017 *Chemistry and Physics of Lipids* **209** 45

[30] Saleem Q, Lai A, Morales H H and Macdonald P M 2012 *Chemistry and Physics of Lipids* **165** 721

[31] Avilova I A, Smolina A V, Kotelnikov A I, Kotelnikova R A, Loskutov V V and Volkov V I 2016 *Applied Magnetic Resonance* **47** 335

[32] Van Der Spoel D, Lindahl E, Hess B, Groenhof G, Mark A E and Berendsen H J C 2005 *Journal of Computational Chemistry* **26** 1701

[33] Marrink S J, Risselada H J, Yefimov S, Tieleman D P and De Vries A H 2007 *Journal of Physical Chemistry B* **111** 7812

[34] Monticelli L, Kandasamy S K, Periole X, Larson R G, Tieleman D P and Marrink S J 2008 *Journal of Chemical Theory and Computation* **4** 819

[35] De Jong D H, Singh G, Bennett W F D, Arnarez C, Wassenaar T A, Schäfer L V, Periole X, Tieleman D P and Marrink S J 2013 *Journal of Chemical Theory and Computation* **9** 687

[36] Bussi G, Donadio D and Parrinello M 2007 *Journal of Chemical Physics* **126** 014101

[37] Berendsen H J, Postma J P, Van Gunsteren W F, Dinola A and Haak J R 1984 *The Journal of Chemical Physics* **81** 3684

[38] Hess B, Bekker H, Berendsen H J and Fraaije J G 1997 *Journal of Computational Chemistry* **18** 1463

[39] Huang J, Rauscher S, Nawrocki G, Ran T, Feig M, De Groot B L, Grubmüller H and MacKerell A D 2016 *Nature Methods* **14** 71

[40] Darden T, York D and Pedersen L 1993 *The Journal of Chemical Physics* **98** 10089

[41] Parrinello M and Rahman A 1981 *J. Appl. Phys.* **52** 7182